Direct measurement of dipole–dipole/CSA cross-correlated relaxation by a constant-time experiment

Yizhou Liu, James H. Prestegard *

Complex Carbohydrate Research Center, The University of Georgia, 220 Riverbend Road, Athens, GA 30603, USA

ABSTRACT

Relaxation rates in NMR are usually measured by intensity modulation as a function of a relaxation delay during which the relaxation mechanism of interest is effective. Other mechanisms are often suppressed during the relaxation delay by pulse sequences which eliminate their effects, or cancel their effects when two data sets with appropriate combinations of relaxation rate effects are added. Cross-correlated relaxation (CCR) involving dipole–dipole and CSA interactions differ from auto-correlated relaxation (ACR) in that the signs of contributions can be changed by inverting the state of one spin involved in the dipole–dipole interaction. This property has been exploited previously using CPMG sequences to refocus CCR while ACR evolves. Here we report a new pulse scheme that instead eliminates intensity modulation by ACR and thus allows direct measurement of CCR. The sequence uses a constant time relaxation period for which the contribution of ACR does not change. An inversion pulse is applied at various points in the sequence to effect a decay that depends on CCR only. A 2-D experiment is also described in which chemical shift evolution in the indirect dimension can share the same constant period. This improves sensitivity by avoiding the addition of a separate indirect dimension acquisition time. We illustrate the measurement of residue specific CCR rates on the non-myristoylated yeast ARF1 protein and compare the results to those obtained following the conventional method of measuring the decay rates of the slow and fast-relaxing ^{15}N doublets. The performances of the two methods are also quantitatively evaluated by simulation. The analysis shows that the shared constant-time CCR (SCT–CCR) method significantly improves sensitivity.

© 2008 Elsevier Inc. All rights reserved.

1. Introduction

Interference between different relaxation interactions such as DD(dipole–dipole)/CSA(chemical shift anisotropy) and DD/DD has long been observed in NMR [1,2]. Anytime that multiple spin relaxation interactions are modulated by the same motion, or highly correlated motions, the possibility of cross-correlation contributions to spin relaxation arises [3]. Although these effects sometimes represent a complication that needs to be carefully eliminated [4], they can be used to advantage in many situations. In TROSY-type experiments they improve spectral resolution, or enhance sensitivity for experiments involving long transverse ^{15}N relaxation delays [5]. In the CRIPT/CRINEPT experiment they can be used for enhancing polarization transfer and improving sensitivity [6]. In certain situations they can be used to retrieve significant structural information [7,8]. Another very common use in protein NMR is the extraction of motional correlation times from the interference of ^{15}N–^{1}H DD and ^{15}N CSA interactions [9–

11]. Many other spin relaxation measurements are, of course, capable of yielding information on motional correlation times. The unique feature of cross-correlated relaxation (CCR) is that interference between two distinct relaxation interactions involving a given coherence can usually be distinguished from other sources of relaxation on the same coherence, making these measurements a preferred route to global or internal motions. Presented here is a new experiment that allows a direct measurement of the ^{15}N DD-CSA transverse cross-correlation rates in proteins with improved sensitivity.

Measurement of transverse interference between ^{1}H–^{15}N DD and ^{15}N CSA interactions is typically based on the cross-relaxation between the Cartesian operators $N_\pm$ and $2H_zN_\pm$, or on the differential self-relaxation of the ^{15}N doublets. The cross-relaxation between $N_\pm$ and $2H_zN_\pm$ is measured by comparison of their relative intensities after a transfer period during which J coupling has to be refocused [10]. The original implementation requires two independent experiments that select for either in-phase or anti-phase coherence so the spectra need to be scaled carefully to correct for the differences in pulse sequences. The scaling issue can be circumvented by symmetrical reconversion that aims at canceling out

* Corresponding author. Fax: +1 706 542 4412.
  E-mail address: jpresteg@ccrc.uga.edu (J.H. Prestegard).

the effects of differential relaxation and pulse imperfections by combining a larger number of independent measurements [12].

Other experiments utilize the differential relaxation rates of the ^{15}N doublets due to DD/CSA interference. The downfield component $H^\alpha N_\pm$ ($0.5N_\pm - H_z N_\pm$) relaxes at the difference of an ACR (λ) and a CCR (η) while the upfield component $H^\beta N_\pm$ ($0.5N_\pm + H_z N_\pm$) relaxes at the sum. Thus CCR can be obtained by taking the difference of the two rates that are separately measured from build-up curves such as in the spin-state selection (S3E-CCR) [13] and TRACT experiments [9], or from the intensity ratio of the up- and downfield peaks of the ^{15}N doublets such as in the constant-time IP and IPAP experiments [14]. With the exception of the constant-time IP experiment which is applicable to small systems with minimal signal overlap, generally two independent measurements are required, which consumes spectrometer time and makes the measurement more susceptible to spectrometer instabilities and non-idealities in the pulse sequences. The need for multiple measurements arises because ACR is not actively blanked in the pulse sequence. Here it is shown that it is possible to directly measure CCR from a mono-exponential decay utilizing a constant-time experiment in which relaxation due to ACR remains invariant. This SCT–CCR method has improved sensitivity compared to previous approaches and is suitable for investigation of large molecules.

As an illustration of the method the residue specific CCRs of the ADP ribosylation protein from yeast (yARF1) are measured and compared with the results obtained using a previous approach of measuring $\lambda + \eta$ and $\lambda - \eta$ separately such as in S3E-CCR and TRACT. yARF1 is a 21.5 kDa, normally myristoylated, protein that is an important regulator of vesicle trafficking [15]. There are a number of issues relating to its aggregation state in both myristoylated and non-myristoylated forms, and its tendency to interact with vesicle membranes, that might be addressed through the measurement of motional correlation times. ^{15}N–^{1}H NMR data have been reported on the non-myristoylated human protein previously [16]. However, an inability to prepare adequate amounts of myristoylated human protein has dictated initiation of work with the yeast protein. The data presented here suggested that the non-myristoylated yeast protein is monomeric at ∼0.5 mM concentration if a rigid-body model is assumed. Using experimental data on the non-myristoylated system as a starting point, the accuracy and robustness of SCT–CCR has been further tested with synthetic data. The results suggest utility in the further study of myristoylated and membrane associated forms of the protein.

2. Pulse sequence design

For convenience, here and in the following text, we define λ as the effective auto-correlation rate, which includes the relaxation due to ^{15}N–^{1}H DD interaction, ^{15}N CSA, DD interaction with remote spins, and chemical exchange, and we define η as the CCR.

The SCT–CCR pulse sequence resembles a constant/semi-constant-time sensitivity enhanced HSQC experiment (Fig. 1) with the following major differences. First, the reverse-INEPT (from point e to detection) adapts the pulse phases proposed by Nietlispach [17] and thus only selects for the slow relaxing downfield (TROSY) component. This scheme has improved sensitivity compared to the original TROSY sequence [18].

Second, the constant period T (between b and d) is constructed so that the eventually detected signal undergoes fast upfield relaxation ($\lambda + \eta$) during the first part of the relaxation period ($\varDelta$) and switches to slow downfield relaxation ($\lambda - \eta$) during the relaxation period after the composite 180° proton inversion pulse ($T - \varDelta$). The ^{15}N refocusing pulses allow ^{15}N chemical shift to evolve for a total time of $\kappa \cdot t_1$ and J coupling for $(1 - 2\varDelta/T) \cdot \kappa \cdot t_1$.

Third, the delay between d and e allows additional ^{15}N frequency labeling by $(1 - \kappa) \cdot t_1$. The scaling factor κ can be chosen according to Eq. (1). For small or medium-sized proteins, T can be set long enough for a t_1 constant-time experiment with κ set to 1. For large proteins at high fields, it may be preferable to use a constant delay T shorter than the desired ^{15}N chemical shift acquisition time $t_{1,\max}$. In this case κ is set to $T/t_{1,\max}$ for a semi-constant-time setup to ensure adequate digitization. This pulse sequence also allows separate measurement of down or upfield magnetization relaxation rates when T is incremented with both κ and $\varDelta$ set to 0, or when T and $\varDelta$ are co-incremented with equal values with only κ set to 0. This implementation is expected to be more sensitive than S3E-CCR and TRACT because t_1 labeling is done under slow downfield relaxation in both measurements, although an imperfect proton inversion pulse may degrade the performance to some extent. For convenience we will refer to this approach in the following text as T-aT (meaning TROSY-anti-TROSY, following the terminology of the TROSY experiment to which our pulse sequence is closely related).

$$\kappa = \begin{cases} 1 & T \geqslant t_{1,\max} \\ \frac{T}{t_{1,\max}} & T < t_{1,\max} \end{cases} \tag{1}$$

Fourth, the reverse-INEPT used here causes measurable amplitude imbalance between real and imaginary parts of the t_1 hypercomplex pair due to the difference between longitudinal and transverse relaxation rates. This allows an unwanted multiplet component to leak through the coherence selection gradients with an intensity equal to half the difference of the real and imaginary amplitudes. We have observed this effect in the yARF1 protein. It gets increasingly pronounced when $\varDelta$ gets closer to T, because the signals to be suppressed have stayed increasingly longer at the slow relaxing rate. The spin-state selection filter between the INEPT and the constant delay T (between a and b) suppresses such artifacts. This scheme was previously adopted by Pervushin et al. [19] and Yang et al. [20] as an alternative way of suppressing anti-TROSY lines. Here the pulse phases have been modified to eliminate the TROSY signal because the composite proton inversion pulse during T imposes a spin flip. This filter also serves to suppress errors from the differential ^{15}N in-phase and anti-phase relaxation, which is detailed in Appendix A.

The product operator analysis of the above experiment is most convenient in the single element operator basis. If we consider only the non-filtered part corresponding to the upfield magnetization, the density operator at point b of Fig. 1 is:

$$\sigma_b = H^\beta N_y \tag{2}$$

The ^{15}N equilibrium magnetization adds constructively to this transition to improve sensitivity. During $\varDelta$ from points b to c, chemical shift and J coupling are partially refocused by the ^{15}N π pulse and active only for $\varDelta / T \cdot \kappa \cdot t_1$. Thus Eq. (2) evolves under fast relaxation as the sum of λ and η to:

$$\sigma_c = -\left(H^\beta N_y \cdot \cos\left[(\Omega_N + \pi J) \frac{\varDelta \cdot \kappa \cdot t_1}{T} \right] + H^\beta N_x \cdot \sin\left[(\Omega_N + \pi J) \frac{\varDelta \cdot \kappa \cdot t_1}{T} \right] \right)$$
$$\cdot \exp(-(\lambda + \eta) \cdot \varDelta) \tag{3}$$

Here Ω_N represents a chemical shift offset in radians/s and J is the N–H spin coupling in Hz. Then the composite inversion pulse flips the proton spin state from β to α and, thus, converts the upfield magnetization to downfield magnetization. During the following $T - \varDelta$, the magnetization undergoes slow downfield relaxation of $\lambda - \eta$. Chemical shift and J coupling evolve for $\pm(T - \varDelta)/T \cdot \kappa \cdot t_1$, respectively. At the end of the constant period (point d), the density operator is described by
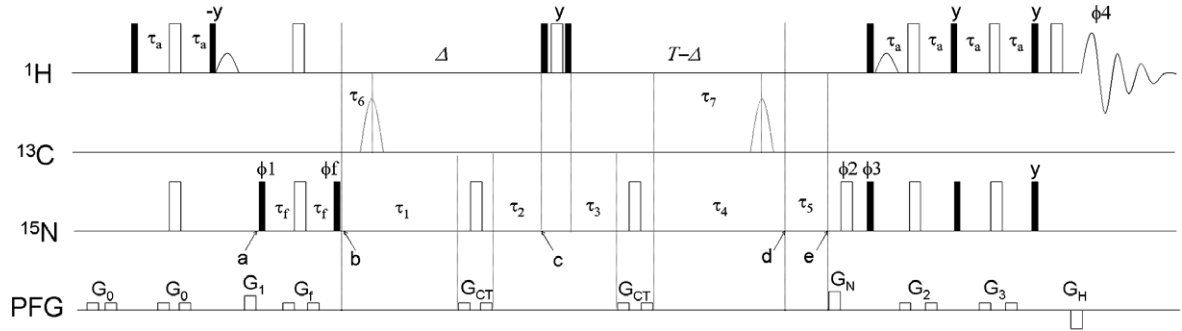
Fig. 1. Pulse sequence of the SCT–CCR experiment. Narrow solid and wide open bars represent 90° and 180° rf pulses, respectively. The rf pulse phase is x unless otherwise indicated. The delays in the solid bracket are: $\tau_1 = \Delta/2 + \Delta/(2T)\cdot\kappa\cdot t_1 + 2\cdot pwH$, $\tau_2 = \Delta/2 - \Delta/(2T)\cdot\kappa\cdot t_1$, $\tau_3 = (T-\Delta)/2 - (T-\Delta)/(2T)\cdot\kappa\cdot t_1$, $\tau_4 = (T-\Delta)/2 + (T-\Delta)/(2T)\cdot\kappa\cdot t_1 + 2\cdot pwH$, $\tau_5 = (1-\kappa)\cdot t_1$, $\tau_6 = \Delta/(2T)\cdot\kappa\cdot t_1 pwH - pwC_{adb}$, $\tau_7 = (T-\Delta)/2 + (1-\kappa)/2\cdot t_1 + pwH - pwC_{adb}$, $\tau_f = 1/(8J_{NH}) \approx 1.2$ ms, $\tau_a = .91/(4J_{NH}) \approx 2.45$ ms. The extra delay of 2 times 90° proton pulse width ($2\cdot pwH$) in τ_1 and τ_4 eliminates phase errors from the composite proton inversion pulse. The two adiabatic $C'-C^\alpha$ refocusing pulses with bandwidth of 200 ppm and duration of 1 ms ($2\cdot pwC_{adb}$) are applied only when $\tau_6 > 0$ and $\tau_7 > 0$, respectively. The *sinc* water flip-back pulse has a duration of 1.4 ms. The shaped pulses and delays are optimized for 600 MHz magnet. The phase cycling is: $\phi_1 = \{3\pi/4, 7\pi/4\}$, $\phi_2 = \{2(x), 2(-x)\}$, $\phi_3 = \{x\}$, $\phi_4 = \{x, -x\}$, $\phi_f = \{y, -y\}$. The gradient G_H and the phase of ϕ_3 are inverted along with the echo/anti-echo alternation. The z gradients are: $G_0 = 1.8$ G/cm, 0.5 ms; $G_1 = 26.6$ G/cm, 1 ms; $G_2 = 3.6$ G/cm, 0.5 ms; $G_3 = 5.4$ G/cm, 0.5 ms; $G_N = 31.9$ G/cm, 2 ms; $G_H = 32.3$ G/cm, 0.2 ms; $G_{CT} = 7.1$ G/cm, 0.5 ms; $G_f = 7.1$ G/cm, 0.5 ms; For high Q probes, the gradient strength of G_{CT} may be increased to suppress radiation damping.

$$\sigma_d = (H^\alpha N_y \cdot \cos\left[(\Omega_N + \pi J)\frac{\Delta \cdot \kappa \cdot t_1}{T} + (\Omega_N - \pi J)\frac{(T-\Delta)\cdot\kappa\cdot t_1}{T}\right]$$
$$+ H^\alpha N_x \cdot \sin\left[(\Omega_N + \pi J)\frac{\Delta\cdot\kappa\cdot t_1}{T} + (\Omega_N - \pi J)\frac{(T-\Delta)\cdot\kappa\cdot t_1}{T}\right]$$
$$\cdot \exp(-(\lambda+\eta)\cdot\Delta - (\lambda-\eta)\cdot(T-\Delta))$$
$$= \left(H^\alpha N_y \cdot \cos\left[\left(\Omega_N - \pi J\left(1 - \frac{2\Delta}{T}\right)\right)\cdot\kappa\cdot t_1\right]\right.$$
$$+ H^\alpha N_x \cdot \sin\left[\left(\Omega_N - \pi J\left(1 - \frac{2\Delta}{T}\right)\right)\cdot\kappa\cdot t_1\right]\right)\cdot\exp(-(\lambda-\eta)\cdot T)$$
$$\cdot\exp(-2\eta\cdot\Delta) \tag{4}$$

Following the additional ^{15}N frequency labeling delay between points d and e, chemical shift and J coupling evolve for $\pm(1-\kappa)\cdot t_1$, respectively. At point e, the density operator is described by:

$$\sigma_e = \left(H^\alpha N_y \cdot \cos\left[\left(\Omega_N - \pi J\left(1 - \frac{2\Delta\cdot\kappa}{T}\right)\right)\cdot t_1\right]\right.$$
$$+ H^\alpha N_x \cdot \sin\left[\left(\Omega_N - \pi J\left(1 - \frac{2\Delta\cdot\kappa}{T}\right)\right)\cdot t_1\right]\right)$$
$$\cdot\exp(-(\lambda-\eta)\cdot T)\cdot\exp(-2\eta\cdot\Delta)\cdot\exp(-(\lambda-\eta)\cdot(1-\kappa)\cdot t_1) \tag{5}$$

After the sensitivity-enhanced reverse INEPT, both $H^\alpha N_y$ and $H^\alpha N_x$ are converted to detectable terms. As is apparent from (5), as Δ varies, the signal intensity decays by $\exp(-2\eta\cdot\Delta)$. An attenuation of $\exp(-(\lambda-\eta)\cdot T)$ is encountered due to the constant delay T, which occurs at the slow downfield relaxation rate. For proteins at high magnetic field this constant attenuation can be quite small. The t_1 dependent relaxation from the extra ^{15}N frequency labeling period $\exp(-(\lambda-\eta)\cdot(1-\kappa)\cdot t_1)$ is independent of Δ, thus spectra from different Δ values have identical line-width in the ^{15}N dimension so that peak heights can be used for the extraction of η.

The 2D Fourier-transformed signal occurs at $(\Omega_H + \pi J_{NH}, \Omega_N - \pi J_{NH}\cdot(1 - 2\Delta\cdot\kappa/T))$. As Δ increases from 0 to T, the peak moves from the TROSY peak position $(\Omega_H + \pi J_{NH}, \Omega_N - \pi J_{NH})$ to $(\Omega_H + \pi J_{NH}, \Omega_N - \pi J_{NH}\cdot(1 - 2\kappa))$. This feature could be used to measure J_{NH} couplings, although it is not the primary objective here.

3. Results and discussion

3.1. Evaluation using experimental data

The SCT–CCR experiment was evaluated on the 21.5 kDa ^{15}N yeast ARF1 protein. Assignments for backbone resonances were made using traditional triple resonance methods (CBCANH and CBCA(CO)NH), and assignments have been deposited in the BMRB (Accession #15626). The SCT–CCR experiment was run on a 0.5 mM sample on a 600 MHz Varian spectrometer with a room temperature probe. As a control, η was also measured by the T-aT method with the pulse sequence in Fig. 1 by varying T while Δ and κ are set to 0 (to measure $\lambda - \eta$), or by co-varying T and Δ while κ is set to 0 (to measure $\lambda - \eta$). The SCT data were acquired in ~11 h and the T-aT data in ~22 h. To confirm the equivalency of the two methods, both experiments were run twice with identical settings. The results of these experiments are presented in Fig. 2. Fig. 2A and B compare the results of one SCT–CCR experiment and the two T-aT experiments. It is clear from the slope that identical values are being measured and that deviations in the results appear to be due to random noise. The average deviation is 3.5%. Fig. 2C compares results from the two T-aT experiments. The average deviation proves to be 3.4%, showing that the scatter in results from the two T-aT experiments is indistinguishable from that between the SCT–CCR and T-aT experiments (Fig. 2A and B). This is true despite the fact that twice the acquisition time was devoted to each of the T-aT experiments. Fig. 2D compares results from two identical SCT–CCR experiments where similar error ranges were found as in other comparisons. Mono-exponential decay curves of representative residues are shown in Fig. 2E.

The residue specific rotational correlation times were calculated following the approach of Lee et al. [9] except that here we used the average geometry-dependent CSA value and bond-length determined from the solution state [23,24]. If a rigid-body model is assumed, the CCRs (Fig. 2F) agree with a monomeric state of the protein. It should be mentioned that correlation times determined this way are subject to the site-to-site variants of geometry-dependent CSA, internal motions and rotational anisotropy. A more detailed picture requires measurement of longitudinal CCR (η_z) to remove the CSA dependence through the ratio of transverse and longitudinal CCRs (η_{xy}/η_z) [11]. Under a rigid-body assumption, the rotational diffusion tensor can be determined from the η_{xy}/η_z ratio.

3.2. Evaluation by simulation

The performance of SCT–CCR can be more extensively evaluated with respect to T-aT by simulation. The measurement accuracy of an exponential decay rate depends on a number of factors, including S/N, the number and method of relaxation sampling, the relaxational acquisition time (T), and the value of the decay rate.
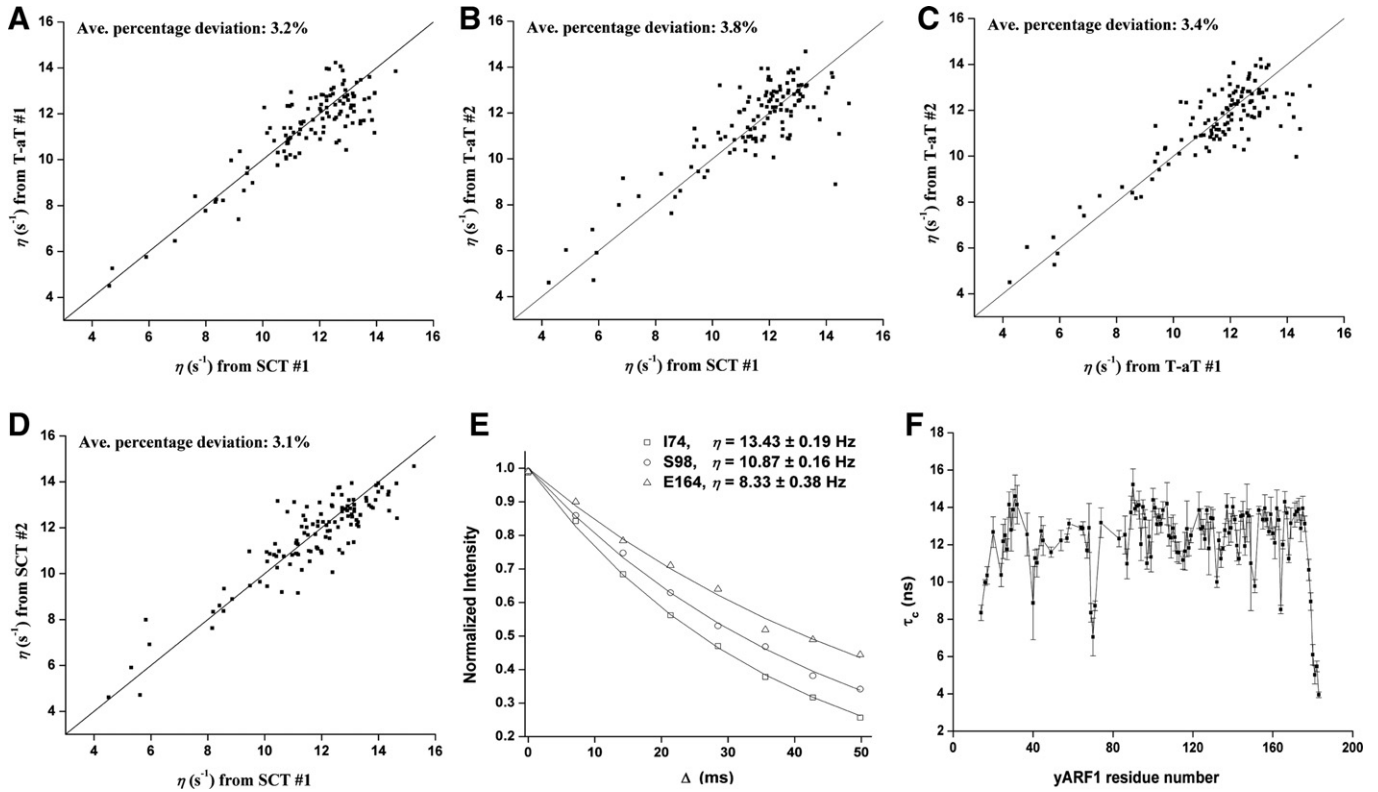
Fig. 2. (A–D) The SCT–CCR experiments were run with $T = 50$ ms, $\kappa = 1$ and $\Delta = (0, 7.12, 14.24, 21.36, 28.48, 35.6, 42.72, 49.84)$ ms, using the pulse sequence in Fig. 1; The T-aT experiments were run with $\kappa = 0$, $T = (0, 20, 40, 60, 80, 100, 120, 140)$ ms, and $\Delta = 0$ ms for TROSY rates, and with $\kappa = 0$ and $\Delta = T = (0, 8, 16, 24, 32, 40, 48, 56)$ ms for anti-TROSY rates. E: Relaxation decay curves of representative residues. F: The rotational correlation times were calculated for non- or mildly overlapping residues in yeast ARF1 protein; the points and error bars correspond to the average values and standard deviations derived from the 4 experiments in (A)–(D).

3.2.1. S/N

In our simulation, we define as unity the intensity of a 2-D Fourier-transformed signal that has undergone no relaxation delay in the TROSY or anti-TROSY rate measurement sequences. The spectral noise is assumed to be random within ±0.05. Thus, the signal intensity of a TROSY/anti-TROSY measurement is modulated by:

$$I(t) = \exp(-R \cdot t) + c \qquad (6)$$

where $R = \lambda \pm \eta$ for up- and downfield relaxation, respectively, and c is the random noise within ±0.05.

Based on this, the intensity of SCT–CCR is simulated from Eq. (5) as:

$$I(t) = g \cdot \exp(-(\lambda - \eta)T) \cdot \exp(-2\eta \cdot t) + c \qquad (7)$$

Here T is the length of the constant delay, t equals Δ in Fig. 1 (thus $t \leqslant T$), and g is the sensitivity gain from sharing the ^{15}N chemical shift evolution within the constant relaxation delay. If a cosine square apodization function is used during data processing of the ^{15}N dimension, the sensitivity gain is [21]:

$$g = \frac{\int_0^{t_{1,max}} \exp(-(\lambda - \eta) \cdot (1 - \kappa) \cdot t) \cdot \cos^2\left(\frac{\pi \cdot t}{2t_{1,max}}\right) dt}{\int_0^{t_{1,max}} \exp(-(\lambda - \eta) \cdot t) \cdot \cos^2\left(\frac{\pi \cdot t}{2t_{1,max}}\right) dt} \qquad (8)$$

where κ is defined by Eq. (1) and $t_{1,max}$ is set to 35 ms in our simulation, although in reality the robustness of mirror image prediction allows a considerably shorter acquisition time to be used [22] in the case where κ is set to 1. It is worth noting that the analysis above is based on the assumption that SCT–CCR consumes half the spectrometer time as T-aT, because in the latter two relaxation rates have to be measured. If we double the transients of SCT–CCR so that both take equal amounts of spectrometer time, the random noise (c in (5)) is lowered by a factor of $\sqrt{2}$.

3.2.2. Sampling

In the simulation, we use uniform sampling with 8 points in total, going from 0 to T.

$$t = \frac{n \cdot T}{7} \quad (n = 0, 1, \ldots, 7) \qquad (9)$$

T is the relaxational acquisition time. In case of SCT–CCR, it is also equal to the constant delay. Geometric sampling is also frequently used in relaxation measurements. Our simulation indicates that for T-aT, linear sampling achieves better accuracy provided T is optimized (data not shown). However geometric sampling is more robust against large mis-setting of T and thus is more favorable in case of very high dynamic ranges of relaxation rates. For SCT–CCR, linear sampling generally gives better accuracy than geometric sampling. In our comparison we focus on the best achievable accuracies of the two different approaches for a given relaxation rate and thus adopt linear sampling in the simulation.

3.2.3. λ and η

To simplify analysis, we consider the spin diffusion limit so that the spectral density function is dominated by the zero-frequency component. Without remote DD interaction and chemical exchange,

$$\begin{cases} \lambda = \left(\frac{\mu_0 \cdot h^2 \cdot \gamma_H^2 \cdot \gamma_N^2}{8(4\pi)^2 r_{HN}^6} + \frac{\Delta\sigma_N^2 \cdot \gamma_N^2 \cdot B_0^2}{18}\right) \cdot 4J(0) \\ \eta = \frac{\mu_0 \cdot h \cdot \gamma_H \cdot \gamma_N}{4\pi \cdot r_{HN}^3} \cdot \frac{\Delta\sigma_N \cdot \gamma_N \cdot B_0}{6} \cdot \frac{3\cos^2\theta - 1}{2} \cdot 4J(0) \end{cases} \qquad (10)$$

Obviously the ratio of λ over η is only dependant on B_0 and certain geometric factors. Here we assume the average ^{1}H–^{15}N geometric and shielding values determined from data on ubiquitin in the solution state apply to all residues; $\Delta\sigma_N = 169$ ppm, $\theta = 21.4°$, and

r_{HN} = 1.04 Å [23,24]. At a 600 MHz field, $\lambda/\eta \cong 1.38$. Remote DD interactions and chemical exchange can be modeled by increasing this ratio. This treatment saves a tremendous amount of simulation time.

3.2.4. The relaxational acquisition time T

The choice of T greatly affects the measurement accuracy in both experiments. During simulation it is incremented from 4 to 200 ms for SCT–CCR, or to 400 ms for T-aT, in 2 ms steps. The value that leads to the smallest standard deviation is defined as T_{best}.

3.2.5. Standard deviational error (SD)

The relaxation rate is calculated by least-square fitting an exponential decay with 8 time points from 0 to T. The standard deviation is estimated from 500 Monte Carlo simulations with the intensity of each sampling point varying randomly within ±0.05. The deviational error of η is propagated according to:

$$SD(\eta) = \begin{cases} \frac{1}{2}SD(2 \cdot \eta) & SCT \\ \frac{1}{2}\sqrt{SD^2(\lambda+\eta) + SD^2(\lambda-\eta)} & \text{T-aT} \end{cases} \quad (11)$$

Using the equations above the deviational errors were estimated for η's covering the range observed for yARF1 at their respective T_{best}'s (Fig. 3A–C). The ratio λ/η was set to 1.38, 2.0, and 2.5 in Fig. 3A–C,

respectively, reflecting increasing contributions from remote DD interactions and chemical exchange at a 600 MHz field. SCT–CCR simulations were conducted for three cases. In the first one, the random spectral noise was set at ±0.05 as was used for T-aT simulations. In the second case, the noise level was lowered to ±0.05/$\sqrt{2}$ reflecting a doubled number of transients so that it would consume an equal amount of spectrometer time as T-aT. In the third case, the noise was set to a level that gives similar accuracies as T-aT in the examined range, which is 0.05/$\sqrt{1.2}$ according to the simulation.

There are several noteworthy trends seen in Fig. 3A–C. The SCT–CCR experiment at half the time slightly under-performs the T-aT experiment (e.g., ~5.4% vs ~5.0% when λ/η=1.38) over a wide range of cross-correlation rates. The SCT–CCR experiment with doubled transients (thus equal time as T-aT) gives significantly better accuracies. SCT–CCR with 1.2-fold transients gives similar accuracies as T-aT, thus saving 40% spectrometer time. The performances of both methods are somewhat insensitive to η within the examined range. The performances of both methods degrade as the ratio of λ/η increases.

The improvement of the SCT–CCR experiment over the T-aT experiment is worth further analysis. Although some signal attenuation is encountered during the constant delay T, this effect is mitigated by the fact that the decay is by the slow relaxation rate
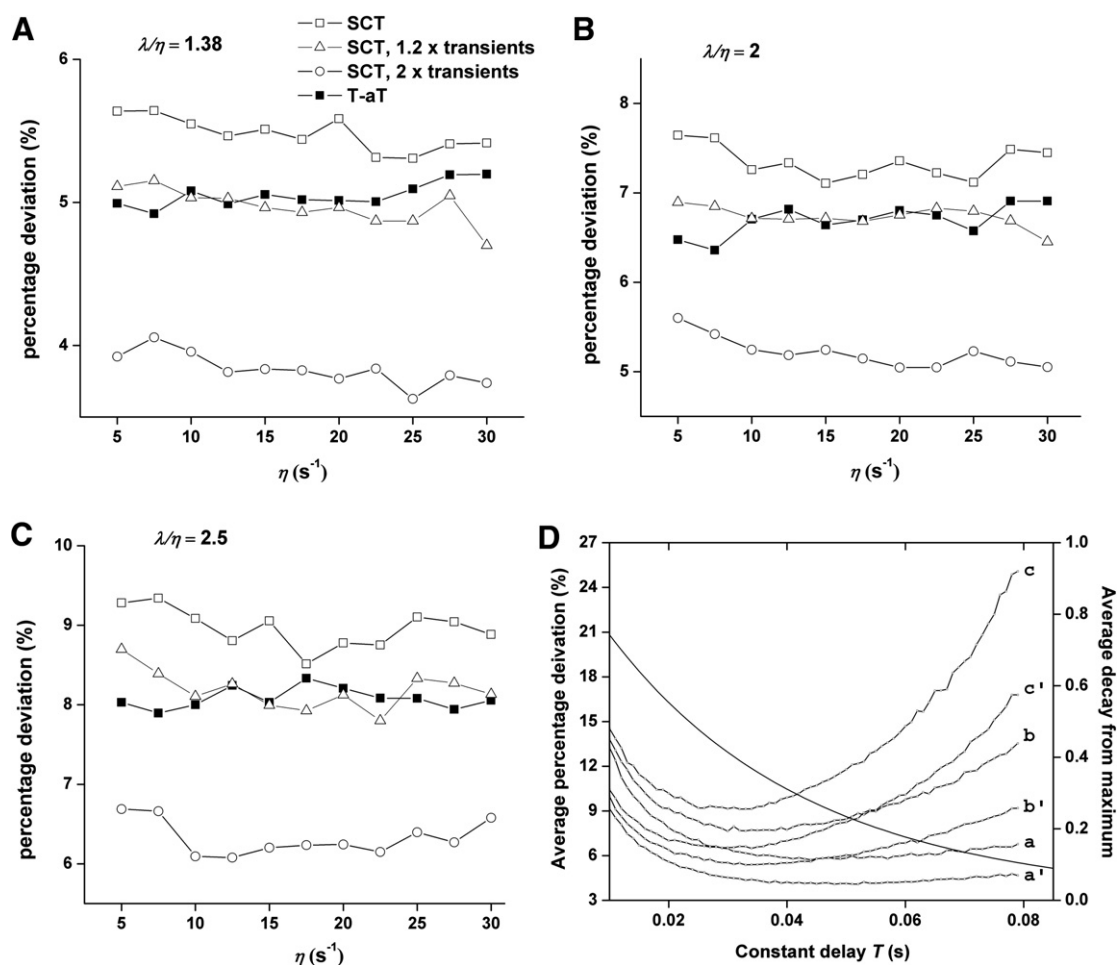

Fig. 3. (A–C) The percentage deviation at T_{best} (minimal percentage deviation) as a function of η for λ/η = 1.38, 2, and 2.5. Data synthesis follows Eqs. (6)–(9). Deviation propagation follows Eq. (11). For T-aT simulations, T_{best} is determined individually for TROSY and anti-TROSY rates. D: Average percentage deviations from CT measurements for η evenly distributed within 10–20 s^{-1}, calculated by $\frac{1}{n}\sum_{i=1}^{n}\frac{SD(\eta_i)}{\eta_i}$, where n = 11, and 10–20 s^{-1}. a: λ/η = 1.38; a′: λ/η = 1.38, double transients; b: λ/η = 2; b′: λ/η = 2, double transients; c: λ/η = 2.5; c′: λ/η = 2.5, double transients; e: decay from the initial intensity averaged over 10–20 s^{-1}, using the equation: $e = \frac{1}{n}\sum_{i=1}^{n}\exp(-2 \cdot \eta(i) \cdot T)$, where n = 11, and $\eta(i)$ = 10,…,20 s^{-1}. It represents the intensity ratio of the last point ($\Delta = T$) over the first point ($\Delta = 0$). The attenuation of $\exp(-(\lambda - \eta) \cdot T)$ in Eq. (5) is irrelevant here and not considered.

of $\lambda - \eta$ (Eq. (5)). Also, sharing ^{15}N chemical shift evolution with the constant delay remedies some of the signal loss, improving sensitivity by $\sim$17% for the yeast ARF1 protein when a cosine square apodization function is used. The percentage is higher in the case of a weaker damping function, such as a cosine function. In addition, the errors are propagated differently in the two methods (Eq. (11)). In the T-aT experiment, the TROSY and anti-TROSY measurements have identical percentage deviation (data not shown) because both decay from the same initial intensity. However, the anti-TROSY measurement gives significantly higher absolute deviation, because its signal decays at $\lambda + \eta$ while in the TROSY measurement it decays at $\lambda - \eta$. As is obvious from Eq. (11), it is the absolute deviation that gets propagated to the uncertainty in η. As a result, the large anti-TROSY rate is the main source of error in the T-aT experiment. In the SCT experiment, the signal decays at 2η, which is significantly smaller than $\lambda + \eta$; this also lowers the absolute deviation. Finally, the SCT–CCR experiment saves time by avoiding two separate measurements, which is equivalent to increased sensitivity.

In the analysis above, we examined the uncertainty at T_{best} for a given pair of λ and η rates. In reality, the molecule under investigation may have a high dynamic range of cross-correlation rates due to anisotropic tumbling or internal motions. Obviously a single relaxational acquisition time T cannot simultaneously be ideal for all the correlation rates. In Fig. 3D, the average percentage deviations (see figure legends for definition) for a uniform distribution of η values spanning the range of 10–20 s^{-1} as a function of T is considered. The curves a/a′–c/c′ correspond to different λ/η values calculated with either equal or twice the number of transients as in T-aT. The minima in the curves correspond to a best averaged T, and the extremes show the effects of not selecting an optimum value. Curve e illustrates the average decay of signal during the experiment. Comparison of Fig. 3A–C vs 3D suggests that the minimal averaged deviation is only slightly higher than the minimal deviation of a single η. Thus the SCT–CCR method is able to handle a range of internal and anisotropic dynamic effects very well.

Lastly, an analysis of how the choice of T impacts the performance is considered. This has considerable practical significance. As shown in Fig. 3D, when the λ/η ratio is low, the performance is stable over a wide range of T values. When the ratio is high, the average deviations go up quickly as T shifts away from the optimized value. In this case it is critical to have an estimate close to optimal before the experiment starts. Under our simulation conditions, near optimal performance occurs when the signal at $\varDelta = T$ is allowed to decay to $\sim$40% of the initial intensity at $\varDelta = 0$, regardless of the λ/η ratio and S/N (Fig. 3D). Similar analysis on η distributed over 20–30 s^{-1} leads to the same conclusion (data not shown). A higher S/N merely scales down the deviation and flattens the curve, but does not change the optimal T value (Fig. 3D). Thus 40% serves as a useful guide during the experiment setup. This value can be quickly selected by observing intensities in several 1-D scans. It is worth mentioning that the 40% guide should be applied to a part of the 1-D spectrum that lacks signals from the flexible terminal regions which relax slowly and are usually not of interest.

3.3. Potential sources of systematic errors

3.3.1. Cross relaxation between the ^{15}N doublets

In the product operator analysis in the earlier section, cross relaxation between the ^{15}N doublet components has been neglected since in amides $(2\pi J)^2$ is usually much greater than $(R_{2,HN} - R_{2,N})^2$, where $R_{2,N}$ and $R_{2,HN}$ refer to ^{15}N in-phase and anti-phase relaxation. The residual effects could be further quenched by setting all J coupling free evolution delays to multiples of 1/2J [25]. However, it is generally not applicable to frequency labeling periods, and the natural spread of couplings

makes this approach less efficient at long delays. Rigorous calculations using the full relaxation matrix are detailed in Appendix A, where it is shown that the spin-state selection filter (between a and b in Fig. 1) employed in SCT–CCR largely suppresses such effects from ^{15}N doublet cross-relaxation. Thus SCT–CCR outperforms the A/B experiment [10] and CT-IP [14] in the presence of fast amide proton longitudinal relaxation.

3.3.2. Cross-correlation between ^{15}N CSA and DD interactions with distant protons

So far we have considered only one pair of nuclei. In actuality the nitrogen can be dipolar coupled to other protons and cross correlation between ^{15}N CSA and these distant DD interactions can also exist. In the SCT–CCR experiment the proton inversion pulse during T has the "side effect" of flipping the spin states of distant protons, which can cause an expected under-estimation by 0.75% for a fully protonated protein based on calculations detailed in Appendix A. These effects are therefore small, but distant relaxation correlations can be further quenched by perdeuteration.

4. Conclusion

Based on the above presentation it is clear that the SCT–CCR experiment has an advantage in sensitivity compared to conventional methods that require two or more complementary measurements. The new method is robust in the presence of a considerable range of cross-correlation rates and is easily adapted to applications where either overall rotational correlation times or the effects of internal motion are of interest. It is robust against the cross-relaxation effect between ^{15}N doublets even in the presence of very high proton longitudinal relaxation. A small and predictable under-estimation occurs associated with proton inversion during the relaxation delay but is usually beyond the resolution of these experiments and can be largely removed by protein perdeuteration.

Acknowledgment

Appendix A. Cross relaxation between the ^{15}N doublets

The magnetization propagates from time 0 (point b, Fig. 1) to T (point d, Fig. 1) by:

$$\begin{pmatrix} \langle H^{\alpha}N_{+}\rangle(T) \\ \langle H^{\beta}N_{+}\rangle(T) \\ \langle H^{\alpha}N_{-}\rangle(T) \\ \langle H^{\beta}N_{-}\rangle(T) \end{pmatrix} = \exp(-\widehat{L}\cdot\tau_4)\cdot R(\pi N)\cdot \exp(-\widehat{L}\cdot\tau_3)\cdot R(\pi H)$$

$$\cdot \exp(-\widehat{L}\cdot\tau_2)\cdot R(\pi N)$$

$$\cdot \exp(-\widehat{L}\cdot\tau_1)\cdot \begin{pmatrix} \langle H^{\alpha}N_{+}\rangle(0) \\ \langle H^{\beta}N_{+}\rangle(0) \\ \langle H^{\alpha}N_{-}\rangle(0) \\ \langle H^{\beta}N_{-}\rangle(0) \end{pmatrix} \quad (A1)$$

where τ_i's are the delays defined in Fig. 1. In the case of on-resonance excitation (i.e., $\Omega_N = 0$), the Liouvillian $\widehat{L}$ is described by:

$$\widehat{L} = \begin{pmatrix} -i\pi J + \overline{R}_2 - \eta & -R_1/2 & 0 & 0 \\ -R_1/2 & i\pi J + \overline{R}_2 + \eta & 0 & 0 \\ 0 & 0 & i\pi J + \overline{R}_2 - \eta & -R_1/2 \\ 0 & 0 & -R_1/2 & -i\pi J + \overline{R}_2 + \eta \end{pmatrix} \quad (A2)$$

where $\overline{R}_2 = (R_{2,N} + R_{2,HN})/2$, $R_1 = R_{2,HN} - R_{2,N}$. $R(\pi N)$ and $R(\pi H)$ in Eq. (A1) are rotation matrices describing the effects of ^{15}N and ^{1}H π pulses, which exchanges the magnetization of $H^{\alpha/\beta}N_+$ and $H^{\alpha/\beta}N_-$, and of $H^\alpha N_\pm$ and $H^\beta N_\pm$, respectively. Neglecting relaxation during the rf pulses, they are represented by:

$$R(\pi N) = \begin{pmatrix} 0 & 0 & 1 & 0 \\ 0 & 0 & 0 & 1 \\ 1 & 0 & 0 & 0 \\ 0 & 1 & 0 & 0 \end{pmatrix} \quad R(\pi H) = \begin{pmatrix} 0 & 1 & 0 & 0 \\ 1 & 0 & 0 & 0 \\ 0 & 0 & 0 & 1 \\ 0 & 0 & 1 & 0 \end{pmatrix} \quad (A3)$$

When the off-diagonal elements in Eq. (A2) are neglected, $H^\alpha N_\pm$ and $H^\beta N_\pm$ evolves independently and Eq. (4) can be trivially derived from Eq. (A1). With the off-diagonal elements included, the analytical solution to Eq. (A2) is extremely complicated so we took a numerical approach based on Eqs. (A1)–(A3). It is clear from Eq. (A1) that the deviation of CCR generally dependents on the experimental settings of T, Δ and t_1. Instead of showing the map of a 3-dimensional grid-search, we only discuss three simple but instructive cases and compare the performance of SCT–CCR with that of CT-IP (CT-coupled-HSQC). The sequential propagation for CT-IP simulation is given by $\exp(-\hat{L} \cdot \frac{T-t_1}{2}) \cdot R(\pi N) \cdot \exp(-\hat{L} \cdot \frac{T+t_1}{2})$ instead of Eq. (A1). A large proton R_1 of 30 s^{-1} is adopted in these simulations along with a J_{NH} coupling of −93 Hz, and η of 12 s^{-1}. $\overline{R}_2$ in Eq. (A2) simply causes an irreversible decay and thus is irrelevant in these comparisons. κ is set to 1 in all cases.

(i) T varies, Δ equals 0 or T, and t_1 equals 0.
η can be determined by: $\log(I_{(\Delta=0,t_1=0)}/I_{(\Delta=T,t_1=0)})/(2T)$. For the CT-IP experiment η is calculated from: $\log(I_{up}/I_{down})/(2T)$,

where T is allowed to vary and t_1 is 0. As shown in Fig. A1A, SCT–CCR is significantly more robust than CT-IP against a random setting of T.

(ii) t_1 varies, T is fixed, and Δ equals 0 or T.
Similarly, η is determined by: $\log(I_{(\Delta=0,t_1)}/I_{(\Delta=T,t_1)})/(2T)$. Comparison can be made to CT-IP where t_1 instead of T is allowed to vary. Results are shown in Fig. A1B. T is set to 0.053 s in both, representing a roughly identical initial deviation at $t_1 = 0$, according to Fig. A1A. SCT–CCR is significantly less sensitive to the incrementing t_1. It is interesting to note from the CT-IP data that varying the position of the ^{15}N refocusing pulse inside a constant delay can cause considerable fluctuations, although Fourier transform of this dimension at a later time should average them out to certain extent.

(iii) T is fixed, t_1 equals 0, and Δ varies between 0 and T.
For CT-IP, T is varied with t_1 set to 0, which is identical to case (i). No direct comparison can be made in this case because different time variables are being changed. However, since both methods assume a mono-exponential modulation by η, namely $\exp(-2\Delta \cdot \eta)$ and $\exp(-2T \cdot \eta)$, here we compare their respective deviations from an ideal mono-exponential curve, as shown in Fig. A1C. The profile of SCT–CCR is indistinguishable from an ideal mono-exponent at the displayed scale while that of CT-IP shows considerable fluctuations, which, of course, synchronize with those seen in Fig. A1A.

The differential performance between the two is because that the coherences are prepared differently prior to the relaxation delay. CT-IP starts with an equal mixture of up and downfield magne-
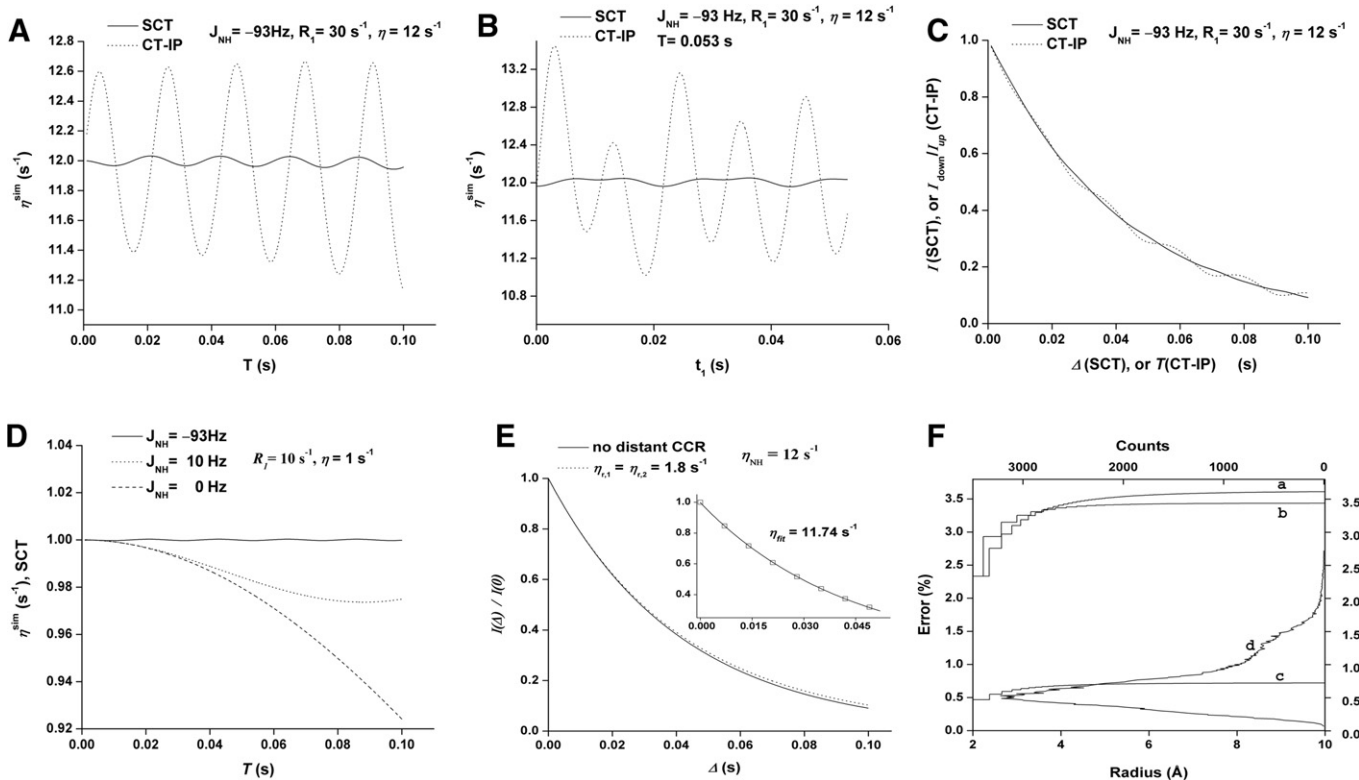

Fig. A1. (A–C) Performance comparisons between SCT–CCR and CT-IP in the presence of high proton longitudinal relaxation. D: Effects of small or zero J couplings in the presence of high proton longitudinal relaxation. E: Estimation of errors due to DD/CSA CCR between amide ^{15}N and two α protons of a glycine residue. F: Estimation of errors with all distant DD/CSA CCR in consideration. a: Error-radius dependence based on the proton density seen in yARF1 and even distribution, with uniform DD/CSA orientation at $\theta = 0$. b: Error-radius dependence based on the proton density around the amide ^{15}N of a glycine and even distribution, with uniform DD/CSA orientation at $\theta = 0$. c: Averaged error-radius profile from 200,000 simulations with random DD/CSA orientation given by $P(\theta) = \frac{\sin(\theta)}{2} \cdot d\theta$, based on the proton density seen in yARF1 and even distribution, d: Histogram of error distribution from 200,000 simulations used in c.

tization: $2H_zN_{x/y} = -H^\alpha N_{x/y} + H^\beta N_{x/y}$, which can be represented by a vector $(-1 - i, 1 + i, 0, 0)$ following the format in Eq. (A1). In contrast, the spin-state selection filter in SCT–CCR (between points a and b in Fig. 1) creates an active coherence solely of the upfield magnetization $H^\beta N_{x/y}$, represented by $(0, 1 + i, 0, 0)$. This largely suppresses the effects due to cross-relaxation between the doublets. Similarly, the S3E-CCR experiment is also expected to perform well in this aspect. For CT-IPAP which contains two experiments with the starting magnetizations described by $(-1 - i, 1 + i, 0, 0)$ (IP) and $(1 + i, 1 + i, 0, 0)$ (AP), the deviations go in opposite directions for the two measurements (data not shown) and thus can be suppressed by post-acquisition addition and subtraction as are normally conducted in these experiments.

A.1. Cross-correlation between ^{15}N CSA and DD interactions with distant protons

Taking into consideration the cross-correlations between ^{15}N CSA and DD interactions with distant protons, the amide down and upfield parts of the density matrix can be expanded as:

$$\sigma_{d/u}(0) = H_N^{\alpha/\beta} N_\pm \cdot I = H^{\alpha/\beta} N_\pm \cdot \sum_{S(i)=\alpha,\beta} \prod_{i=1}^{n} H_i^{S(i)} \tag{A4}$$

where I is the identity operator, i refers to the i-th remote proton and $S(i)$ is the spin state of the i-th proton. The nitrogen is dipolar coupled to n distant protons so we expand the original 2-spin operator into 2^n $n + 2$ spin operators in the direct product space. To simplify analysis, we neglect cross-relaxation among these operators due to proton R_1's so that these 2^n operators relax independently at their respective rates. This approach can be validated from Fig. A1D, which shows that a high proton R_1 of 10 s^{-1} has very small effects on the effective CCR even in the absence of J coupling within the time-scale used for transverse CCR measurements. Cross-correlations between different DD interactions are not affected by the proton inversion pulse and are therefore not considered. Thus the evolution of these operators obey:

$$\sigma_{d/u}(t) = H_N^{\alpha/\beta} N_\pm \cdot \sum_{S(i)=\alpha,\beta} \prod_{i=1}^{n} H_i^{S(i)}$$

$$\cdot \exp\left(-\left(\lambda \mp \eta + \sum_{i=1}^{n} \eta_i(1 - 2\delta_{S(i),\alpha})\right) \cdot t\right)$$

$$= H_N^{\alpha/\beta} N_\pm \cdot \exp(-(\lambda \mp \eta) \cdot t) \cdot \frac{1}{2^n} \cdot \prod_{i=1}^{n} (\exp(\eta_i \cdot t)$$

$$+ \exp(-\eta_i \cdot t)) + O(t) \tag{A5}$$

where $\delta_{S(i),\alpha}$ is the Kronecker delta. The second line of Eq. (A5) is obtained using the relationship: $H_i^{\alpha/\beta} N_\pm = \frac{1}{2} N_\pm \mp H_{i,z} N_\pm$. $O(T)$ encapsulates all the coherences that are multi-quantum during direct acquisition. In the context of SCT–CCR, the density operator at the end of the constant delay T is described by:

$$\sigma_{SCT}(T) = H^\alpha N_\pm \cdot \exp\left(-\left(\lambda - \eta - \sum_{i=1}^{i=n} \eta_i(1 - 2\delta_{S(i),\alpha})\right)T\right)$$

$$\cdot \exp(-2\eta \cdot \Delta) \cdot \frac{1}{2^n} \prod_{i=1}^{n} (\exp(2\eta_i \cdot \Delta) + \exp(-2\eta_i \cdot \Delta)) + O(T) \tag{A6}$$

The term $\frac{1}{2^n} \prod_{i=1}^{n} (\exp(2\eta_i \cdot \Delta) + \exp(-2\eta_i \cdot \Delta))$ indicates that distant DD/CSA CCRs also modulate with respect to Δ. Taylor expansion of the exponents mutually cancels the odd terms but the even terms add up. Since $(\exp(2\eta_i \cdot \Delta) + \exp(-2\eta_i \cdot \Delta))/2 \geq 1$, the effects from all the remote CCRs accumulate regardless of the signs of η_i, and lead to systematic under-estimation of amide CCR. The percentage error

associated with a measurement of two sampling points at Δ_1 and Δ_2 is:

$$PE = \frac{1}{2 \mid \Delta_1 - \Delta_2 \mid \cdot \eta} \cdot \sum_{i=1}^{n} \log\left(\frac{\exp(2\eta_i \cdot \Delta_2) + \exp(-2\eta_i \cdot \Delta_2)}{\exp(2\eta_i \cdot \Delta_1) + \exp(-2\eta_i \cdot \Delta_1)}\right) \tag{A7}$$

Due to the r^{-3} dependence of CCR, these correlations are usually quite weak. Glycine is the most likely to be affected which has two α protons just over 2 Å away from the amide nitrogen. Assuming an η_{HN} of 12 s^{-1} with $\theta = 0°$ for the amide proton and 0° for α protons as a conservative estimate, CCR to the two α protons is around 1.8 s^{-1} each. The deviation from the ideal mono-exponent is shown in Fig. A1E. An 8 point linear sampling from 0 to 0.049 s leads to a η of ~11.74 s^{-1}, or ~2.2% under-estimation. As the ^1H–^{15}N distance increases, the contribution sharply drops. Similar calculations indicate that it takes 10 protons at 3 Å, or 209 protons at 5 Å to cause 1% error, either of which is extremely unlikely.

An upper limit of error can be estimated that combines the effects from all distant protons. This is conducted in two ways. One is based on the ARF protein which has a radius of ~20 Å and contains ~1500 protons. A proton distance profile is generated assuming even distribution. The other approach starts with a glycine that has 2 protons within 2 Å and assumes the number of protons at distance r to ^{15}N is proportional to r^2. In both calculations, we gradually (0.001 Å step-size) increase the radius of a sphere from 2 Å with ^{15}N in the center, and incorporate the effects of newly encompassed protons. The compound errors are calculated based on Eq. (A7) with $\Delta_1 = 0$ and $\Delta_2 = 0.04$ s, and $\theta = 0°$, which represents the least favorable DD/CSA geometry. As shown in Fig. A1F curves a and b which result from the two approaches, respectively, the percentage error is quickly saturated at ~5 Å to a final value of ~3.5%. Also shown in Fig. A1F (curves c and d) is a simulation based on a true random distribution with the probability density at θ equal to $\sin(\theta)/2$. Curve c is a profile averaged over 200,000 simulations and curve d is a histogram showing the probability distribution for the observed error range, which mimics a chemical shift powder pattern. These simulations show that the probability-weighted average ("isotropic" value) is about 0.75% and it is extremely rare to have an error above 2%. Generally errors of this magnitude are not a concern and are paid off by the enhanced sensitivity of this method. Moreover, if the protein structure is known, this error can be readily predicted. The modulation by distant DD/CSA CCRs can be quenched by replacing the hard proton inversion pulse in the relaxation delay with a band-selective pulse covering the amide region, although modulations from DD/DD CCRs will arise instead. Protein perdeuteration should be a better solution.

References

[1] E.L. Mackor, C. Maclean, Sign of J_{HF} in CHFCl$_2$, J. Chem. Phys. 44 (1966) 64–69.
[2] J.H. Prestegard, D.M. Grant, Characterization of anisotropic motion in fatty acid micelles by analysis of transverse relaxation in an AX$_2$ nuclear spin system, J. Am. Chem. Soc. 100 (1978) 4664–4668.
[3] M. Goldman, Interference effects in the relaxation of a pair of unlike spin-1/2 nuclei, J. Magn. Reson. 60 (1984) 437–452.
[4] A.G. Palmer III, N.J. Skelton, W.J. Chazin, P.E. Wright, M. Rance, Suppression of the effects of cross-correlation between dipolar and anisotropic chemical shift relaxation mechanisms in the measurement of spin–spin relaxation rates, Mol. Phys. 75 (1992) 699–711.
[5] K. Pervushin, R. Riek, G. Wider, K. Wüthrich, Attenuated T2 relaxation by mutual cancellation of dipole–dipole coupling and chemical shift anisotropy indicates an avenue to NMR structures of very large biological macromolecules in solution, Proc. Natl. Acad. Sci. USA 94 (1997) 12366–12371.
[6] R. Riek, G. Wider, K. Pervushin, K. Wüthrich, Polarization transfer by cross-correlated relaxation in solution NMR with very large molecules, Proc. Natl. Acad. Sci. USA 96 (1999) 4918–4923.
[7] B. Reif, M. Hennig, C. Griesinger, Direct measurement of angles between bond vectors in high-resolution NMR, Science 276 (1997) 1230–1233.
[8] D. Yang, R. Konrat, L.E. Kay, A multidimensional NMR experiment for measurement of the protein dihedral angle ψ based on cross-correlated relaxation between ^1H–^{13}C dipolar and $^{13}C'$ (carbonyl) chemical shift anisotropy mechanisms, J. Am. Chem. Soc. 119 (1997) 11938–11940.

[9] D. Lee, C. Hilty, G. Wider, K. Wüthrich, Effective rotational correlation times of proteins from NMR relaxation interference, J. Magn. Reson. 178 (2006) 72–76.

[10] N. Tjandra, A. Szabo, A. Bax, Protein backbone dynamics and ^{15}N chemical shift anisotropy from quantitative measurement of relaxation interference effects, J. Am. Chem. Soc. 118 (1996) 6986–6991.

[11] C.D. Kroenke, J.P. Loria, L.K. Lee, M. Rance, A.G. Palmer III, Longitudinal and transverse ^{1}H–^{15}N dipolar/^{15}N chemical shift anisotropy relaxation interference: unambiguous determination of rotational diffusion tensors and chemical exchange effects in biological macromolecules, J. Am. Chem. Soc. 120 (1998) 7905–7915.

[12] P. Pelupessy, G.M. Espallargas, G. Bodenhausen, Symmetrical reconversion: measuring cross-correlation rates with enhanced accuracy, J. Magn. Reson. 161 (2003) 258–264.

[13] P.R. Vasos, J.B. Hall, D. Fushman, Spin-state selection for increased confidence in cross-correlation rates measurements, J. Biomol. NMR 31 (2005) 149–154.

[14] J.B. Hall, K.T. Dayie, D. Fushman, Direct measurement of the ^{15}N CSA/dipolar relaxation interference from coupled HSQC spectra, J. Biomol. NMR 26 (2003) 181–186.

[15] C. D'Souza-Schorey, P. Chavrier, ARF proteins: roles in membrane traffic and beyond, Nat. Rev. Mol. Cell. Biol. 7 (2006) 347–358.

[16] J.C. Amor, R.D. Seidel, F. Tian, R.A. Kahn, J.H. Prestegard, ^{1}H, ^{15}N and ^{13}C assignments of full length human ADP ribosylation factor 1 (ARF1) using triple resonance connectivities and dipolar couplings, J. Biomol. NMR 23 (2002) 253–254.

[17] D. Nietlispach, Suppression of anti-TROSY lines in a sensitivity enhanced gradient selection TROSY scheme, J. Biomol. NMR 31 (2005) 161–166.

[18] D. Yang, L.E. Kay, Improved ^{1}HN-detected triple resonance TROSY-based experiments, J. Biomol. NMR 13 (1999) 3–10.

[19] K. Pervushin, R. Riek, G. Wider, K. Wüthrich, Transverse relaxation-optimized spectroscopy (TROSY) for NMR studies of aromatic spin systems in ^{13}C-labeled proteins, J. Am. Chem. Soc. 120 (1998) 6394–6400.

[20] D. Yang, R.A. Venters, G.A. Mueller, W.Y. Choy, L.E. Kay, TROSY-based HNCO pulse sequences for the measurement of ^{1}HN–^{15}N, ^{15}N–^{13}CO, ^{13}CO–^{13}C$^{\alpha}$ dipolar couplings in ^{15}N, ^{13}C, ^{2}H-labeled proteins, J. Biomol. NMR 14 (1999) 333–343.

[21] R.R. Ernst, G. Bodenhausen, A. Wokaun, Principles of nuclear magnetic resonance in one and two dimensions, Clarendon Press, Oxford, 1987.

[22] G. Zhu, A. Bax, Improved linear prediction for truncated signals of know phase, J. Magn. Reson. 90 (1990) 405–410.

[23] P. Damberg, J. Jarvet, A. Gräslund, Limited variations in ^{15}N CSA magnitudes and orientations in ubiquitin are revealed by joint analysis of longitudinal and transverse NMR relaxation, J. Am. Chem. Soc. 127 (2005) 1995–2005.

[24] G. Cornilescu, A. Bax, Measurement of proton, nitrogen, and carbonyl chemical shielding anisotropies in a protein dissolved in a dilute liquid crystalline phase 122 (2000) 10143–10154.

[25] R. Ghose, J.H. Prestegard, Improved estimation of CSA-dipolar coupling cross-correlation rates from laboratory-frame relaxation experiments, J. Magn. Reson. 134 (1998) 308–314.